ACS Photonics

pubs.acs.org/journal/apchd5

Letter

Theory of Multiple Scattering Enhanced Single Particle Plasmonic Sensing

Joel Berk and Matthew R. Foreman*

Cite This: *ACS Photonics* 2021, 8, 2227–2233

Read Online

ACCESS | Metrics & More | Article Recommendations | Supporting Information

ABSTRACT: Methods to increase the light scattered from small particles can help improve the sensitivity of many sensing techniques. Here, we investigate the role multiple scattering plays in perturbing the scattered signal when a particle is added to a random scattering environment. Three enhancement factors, parametrizing the effect of different classes of multiple scattering trajectories on the field perturbation, are introduced and their mean amplitudes explored numerically in the context of surface plasmon polariton scattering. We demonstrate that there exists an optimum scatterer density at which the sensitivity enhancement is maximized, with factors on the order of 10^2 achievable. Dependence of the enhancement factors on scatterer properties are also studied.

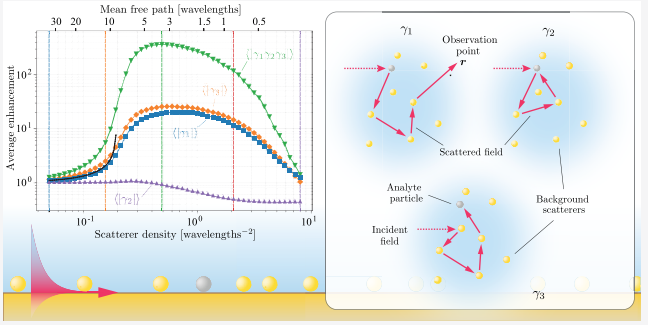

KEYWORDS: *random and disordered media, single particle detection, electromagnetic scattering, surface plasmons*

High sensitivity and label-free optical measurements play a critical role in applications including clinical diagnostics, environmental monitoring, and detection of single nanoparticles.[1,2] Detection strategies employing light scattered from analyte particles, such as dynamic light scattering and interferometric scattering microscopy, have proven highly successful[3−6] with detection of discrete binding events of biomolecules such as proteins,[7,8] virions,[9] DNA,[10] and enzymes,[11] representing one of the ultimate goals in the field. Performance of such systems can, however, significantly degrade in the presence of additional secondary or multiple scattering from the local environment.[12−14] In many systems of experimental interest, for example, colloids or biological tissue, multiple scattering is unavoidable and must thus be accounted for in order to probe them accurately.[15,16] Multiple scattering effects, however, also afford a number of practical gains. For example, the inherent angular spread caused by scattering allows the diffraction limit to be overcome,[17] while random optical speckle patterns have been shown to possess sensitivity to the properties of a single particle,[18,19] in turn, enabling their localization.[20,21] Such potential advantages mean that engineering the photonic scattering environment in order to promote multiple scattering is frequently investigated. Generation of small regions in which the electric field intensity is much larger than the surrounding region, using for example, metallic nanoparticles near metal interfaces,[22,23] or rough metal surfaces,[24] is a common example. Analyte particles in such "hotspots" in turn scatter more light, thereby endowing sensors with a greater sensitivity.[25] Similar hotspot mechanisms have been studied in the context of enhanced fluorescence and Raman scattering.[24,26,27] Carefully designed nanostructured substrates have also received significant attention,[28,29] whereby coupling of different nanostructures can augment any perturbation upon addition of an analyte particle. Randomly distributed nanostructures are also known to give rise to a rich set of multiple scattering phenomena not seen in deterministic structures, such as Anderson localization and long-range correlations,[30−33] which can aid single particle detection. In combination with the less stringent fabrication requirements, random sensors therefore represent a particularly promising platform for enhanced particle sensing.

In this Letter we consider the origin and magnitude of differing mechanisms, which can enhance single particle sensing in random multiple scattering environments. Three classes of scattering trajectory are analytically identified corresponding to coupling between different scatterers, generation of localized hotspots and scattering induced self-interactions. We show, through numerical modeling of a random nanostructured plasmonic substrate, that competition between different multiple scattering effects, namely, dipolar coupling and localization, provides opportunities to optimize achievable enhancements through variation of the average

Received: May 17, 2021
Published: July 19, 2021

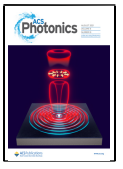

https://doi.org/10.1021/acsphotonics.1c00725
ACS Photonics 2021, 8, 2227–2233

scatterer density and polarizability. Insights gained in this work can, hence, guide the future design of optimal scattering based single particle detectors, in turn, facilitating for instance nonequilibrium biological studies[34] or study of molecular machines.[35]

In order to study a disordered scattering environment, we use a coupled dipole formalism, valid for scattering from small scatterers in which the dipole mode is dominant.[36−38] Typically, the dipole approximation is valid for subwavelength size scatterers and when the field within the scatterer is approximately homogeneous.[39] Initially we consider a system of N dipole scatterers centered at $\boldsymbol{r}_i$ (i = 1, 2, ..., N). When illuminated with a monochromatic electric field $\boldsymbol{E}_0(\boldsymbol{r})$ of frequency ω, the total field $\boldsymbol{E}(\boldsymbol{r})$ at a position $\boldsymbol{r}$ outside the volume of the scatterers is

$$\boldsymbol{E}(\boldsymbol{r}) = \boldsymbol{E}_0(\boldsymbol{r}) + \frac{k_0^2}{\varepsilon_0}\sum_{j=1}^{N} G(\boldsymbol{r}, \boldsymbol{r}_j)\boldsymbol{p}_j \tag{1}$$

where $k_0 = \omega/c$ is the free-space wavenumber, c is the speed of light in a vacuum, ε_0 is the vacuum permittivity, and $G(\boldsymbol{r}, \boldsymbol{r}')$ is the Green's function defined with respect to the background dielectric function $\varepsilon(\boldsymbol{r})$, that is, excluding the N scatterers. Notably, we allow the dielectric function to vary spatially such that our description is applicable to substrate based setups. The dipole moment of the jth scatterer is given by $\boldsymbol{p}_j = \alpha_j \boldsymbol{E}_{\mathrm{exc}}(\boldsymbol{r}_j)$, where α_j is the dressed polarizability including any potential self-interactions (e.g., due to reflections from a substrate) and $\boldsymbol{E}_{\mathrm{exc}}(\boldsymbol{r}_j) = \boldsymbol{E}_0(\boldsymbol{r}_j) + \sum_{i\neq j} G(\boldsymbol{r}_j, \boldsymbol{r}_i)\boldsymbol{p}_i$ is the exciting field incident on the jth dipole, consisting of the incident field and the field from all other dipoles.[36,40] In general, α_j is a tensor, however, reduces to a scalar for isotropic scattering, for example, spherical scatterers in a homogeneous environment. The set of equations $\boldsymbol{p}_j = \alpha_j \boldsymbol{E}_{\mathrm{exc}}(\boldsymbol{r}_j)$ can be expressed as the set of linear equations:

$$\sum_{j=1}^{N} M_{ij}\boldsymbol{p}_j = \boldsymbol{p}_{0,i},\ i = 1, 2, ..., N \tag{2}$$

where $\boldsymbol{p}_{0,i} = \alpha_i \boldsymbol{E}_0(\boldsymbol{r}_i)$ is the dipole moment of the ith scatterer induced solely by the incident field,

$$M_{ij} = \begin{cases} I_3 & i = j \\ -\dfrac{k_0^2}{\varepsilon_0}\alpha_i G_{ij} & i \neq j \end{cases} \tag{3}$$

I_3 is the 3 × 3 identity matrix and for convenience we let $G_{ij} = G(\boldsymbol{r}_i, \boldsymbol{r}_j)$. Formally, the dipole moments are given by $\boldsymbol{p}_i = \sum_{j=1}^{N} M_{ij}^{-1}\boldsymbol{p}_{0,j}$. Note M_{ij}^{-1} denotes the (i,j)th 3 × 3 block (i.e., rows $3i-2$ to $3i$ and columns $3j-2$ to $3j$) of the inverse of the entire $3N \times 3N$ coupling matrix, as opposed to $(M_{ij})^{-1}$, the inverse of the 3 × 3 matrix M_{ij}. In the single scattering regime, interactions between different scatterers are negligible such that $M_{ij} = M_{ij}^{-1} = I_3\delta_{ij}$ and $\boldsymbol{p}_i = \boldsymbol{p}_{0,i}$.

Introduction of an additional scatterer, namely the analyte particle, with polarizability α_{N+1} at position $\boldsymbol{r}_{N+1}$, to the disordered system produces an associated change in the scattered field, $\delta\boldsymbol{E}(\boldsymbol{r})$, given by

$$\delta\boldsymbol{E}(\boldsymbol{r}) = \frac{k_0^2}{\varepsilon_0}G(\boldsymbol{r}, \boldsymbol{r}_{N+1})\boldsymbol{p}_{N+1} + \frac{k_0^2}{\varepsilon_0}\sum_{j=1}^{N} G(\boldsymbol{r}, \boldsymbol{r}_j)\delta\boldsymbol{p}_j \tag{4}$$

The first term in eq 4 corresponds to the additional dipole field originating from the analyte particle, while the second term is the change arising due to the perturbations to the original N dipole moments $\delta\boldsymbol{p}_j$. Analogous expressions for the perturbed field have been derived previously within a scalar model[41] in terms of the determinant of the coupling matrix, however, the vectorial form in eq 4 is more appropriate for electromagnetic problems. Within the single scattering approximation, there is no coupling between dipoles, whereby $\delta\boldsymbol{p} = \boldsymbol{0}$ and the perturbation to the scattered field $\delta\boldsymbol{E}_{\mathrm{ss}}$ reduces to

$$\delta\boldsymbol{E}_{\mathrm{ss}}(\boldsymbol{r}) = \frac{k_0^2}{\varepsilon_0}G(\boldsymbol{r}, \boldsymbol{r}_{N+1})\boldsymbol{p}_{0,N+1} \tag{5}$$

In the full multiple scattering case the perturbation $\delta\boldsymbol{E}$ can be expressed in the same form as eq 5 albeit with a modified dipole moment $\boldsymbol{p}_{0,N+1} \rightarrow \gamma_1\gamma_2\gamma_3\boldsymbol{p}_{0,N+1}$ (see ref 42 for a full derivation), where γ_1, γ_2, and γ_3 are enhancement factors given by

$$\gamma_1 = I_3 + \frac{k_0^2}{\varepsilon_0}G(\boldsymbol{r}, \boldsymbol{r}_{N+1})^{-1}\sum_{i,j=1}^{N} G(\boldsymbol{r}, \boldsymbol{r}_i)M_{ij}^{-1}\alpha_j G_{j,N+1} \tag{6}$$

$$\gamma_2 = \left[I_3 - \frac{k_0^4}{\varepsilon_0^2}\sum_{i,j=1}^{N} \alpha_{N+1}G_{N+1,i}M_{ij}^{-1}\alpha_j G_{j,N+1}\right]^{-1} \tag{7}$$

$$\gamma_3 = I_3 + \frac{k_0^2}{\varepsilon_0}\sum_{i,j=1}^{N} \alpha_{N+1}G_{N+1,i}M_{ij}^{-1}\frac{\boldsymbol{p}_{0,i}\boldsymbol{p}_{0,N+1}^{\dagger}}{|\boldsymbol{p}_{0,N+1}|^2} \tag{8}$$

All multiple scattering effects are captured in the three enhancement factors. In general, γ_i (i = 1, 2, and 3) are complex matrices, reflecting the fact that multiple scattering can modify the amplitude, phase and polarization of the scattered field. An estimate of the relative magnitude of the change in the scattered field resulting from multiple scattering $|\delta\boldsymbol{E}|/|\delta\boldsymbol{E}_{\mathrm{ss}}|$ can be found by considering $\|G(\boldsymbol{r}, \boldsymbol{r}_{N+1})\gamma_1\gamma_2\gamma_3 G(\boldsymbol{r}, \boldsymbol{r}_{N+1})^{-1}\| \leq \kappa_G\|\gamma_1\gamma_2\gamma_3\| \leq \kappa_G\|\gamma_1\|\|\gamma_2\|\|\gamma_3\|$, where we have used the submultiplicative property of the induced norm and κ_G is the condition number of $G(\boldsymbol{r}, \boldsymbol{r}_{N+1})$ given by the ratio of the maximal and minimal singular values.[43] An important class of problems in which equality of the former bound is achieved is systems in which a scalar description is permissible, whereby all tensor quantities (α_i, G and $\boldsymbol{p}_i$) are replaced with corresponding scalars. In this case, $\kappa_G = 1$ and $|\gamma_1\gamma_2\gamma_3|$ directly represents the scaling of the amplitude of $\delta\boldsymbol{E}$ from multiple scattering effects.

Physically, each enhancement factor γ_i can be associated with a distinct class of multiple scattering trajectories, as shown in Figure 1. Specifically, γ_1 describes the effect of rescattering of light initially scattered by the analyte particle and, hence, corresponds to dipole coupling with the analyte. The set of multiple scattering paths described by γ_2 are closed loops in which light scattered by the analyte particle returns via scattering off of the initial scatterers to the analyte particle. Finally, multiple scattering of the incident field onto the added scatterer, which modifies the field at $\boldsymbol{r}_{N+1}$, is described by γ_3. The hotspot effect would manifest in a large value of $\|\gamma_3\|$. The enhancement factors contain a complete description of every possible multiple scattering path. Note that it is possible that $\|\gamma_i\| < 1$ and, as such, the enhancement factors need not describe an increase in the light scattered to a point. Thus, for

https://doi.org/10.1021/acsphotonics.1c00725
ACS Photonics 2021, 8, 2227−2233

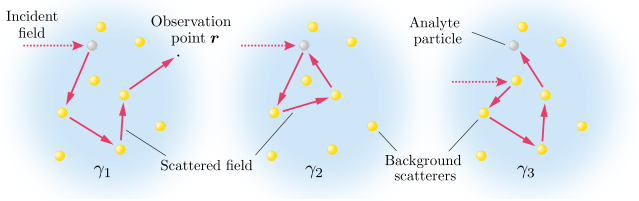

Figure 1. Typical multiple scattering paths associated with each enhancement factor. (left) Rescattering of light en route to the observation point $\boldsymbol{r}$ after scattering from the analyte particle, (center) loop trajectories, and (right) multiple scattering of the illumination field onto the analyte particle.

example, if a particular configuration of scatterers directed light away from the point $\boldsymbol{r}$ after leaving the analyte particle, the second term in eq 6 would (partially) cancel with the first I_3 term such that $\delta\boldsymbol{E}$ is reduced by the scattering paths described by γ_1.

The values of the enhancement factors are determined by the initial scattering configuration (α_i and $\boldsymbol{r}_i$ for $i = 1, ..., N$) and the polarizability and position of the added analyte particle (α_{N+1} and $\boldsymbol{r}_{N+1}$). In reality, however, the exact scattering configuration is rarely known and thus we here study the statistics of the enhancement factors over an ensemble of random configurations. In ref 42, we present an analytic treatment of the mean enhancement factors, however, in this Letter we consider the average magnitude of the enhancement factor, since $\|\gamma_i\|$ is more closely related to experimentally measurable quantities, such as optical intensity. Since a mathematical analysis is not tractable across all scattering regimes, we here use Monte Carlo simulations to study the full range of scatterer densities. For definiteness, we consider multiple scattering of surface plasmon polaritons (SPPs) propagating along a single metal−dielectric interface to illustrate some features of the enhancement factors through evaluation of eqs 6−8. Notably, SPPs are widely used in biosensors[44] and can play a key role in nanostructured substrates.[45] Our example therefore represents an important model system where multiple scattering enhancements can affect single particle sensing and tracking.[6,46] A schematic of the system under consideration is shown in the inset of Figure 2, in which an SPP propagating along a metal−dielectric interface (with permittivities ε_m and ε_d, respectively), is scattered from nanoparticles resting on the substrate (see also ref 46 for further details). SPPs can either scatter into other SPPs propagating in a random direction along the metal surface or into waves propagating away from the surface where they are then ultimately detected in the far-field. A dipole approximation is valid in this system when surface dressing effects are weak as discussed fully in ref 47. In such a system our analysis is especially simplified when $|a| \ll 1$, where $a = [\varepsilon_d/(-\varepsilon_m)]^{1/2}$, because a scalar model can be used to describe SPP scattering.[47,48] Specifically, the relevant scalar field corresponds to the out of plane E_z component of the SPP field, such that only the G_{zz} component of the Green's tensor is considered. The scalar Green's function for points near the surface ($z, z' \ll \lambda_0$) for this model can be approximated as[38,47,49]

$$G_{SPP}(\boldsymbol{r}, \boldsymbol{r}') \approx iA_0 e^{-ak_{SPP}(z+z')} H_0^{(1)}(k_{SPP}|\boldsymbol{\rho} - \boldsymbol{\rho}'|) \quad (9)$$

where $A_0 = ak_{SPP}/[2(1 - a^4)(1 - a^2)]$, k_{SPP} is the complex SPP wavenumber (with corresponding absorption length $l_{abs} = (2\mathrm{Im}[k_{SPP}])^{-1}$) and $H_0^{(1)}(x)$ is the zeroth order Hankel function of the first kind. Equation 9 is thus used to calculate $G_{ij} = G_{SPP}(\boldsymbol{r}_i, \boldsymbol{r}_j)$. The elastic SPP scattering cross-section is then given by $\sigma_{SPP} = 4|\mu|^2/\mathrm{Re}[k_{SPP}]$, where $\mu = \alpha(k_0^2/\varepsilon_0)A_0 \exp[-2ak_{SPP}z_s]$.[48] Throughout this work we define the elastic scattering mean free path as $l_s = (n\sigma_{SPP})^{-1}$, where $n = N/L^2$ is the scatterer density.[50] Although at large densities the mean free path is more accurately defined in terms of the self-energy,[50] we use this parametrization since the closed form greatly facilitates computation. Deviations from the true length scales are expected, albeit we note all calculations are performed with respect to scatterer density.

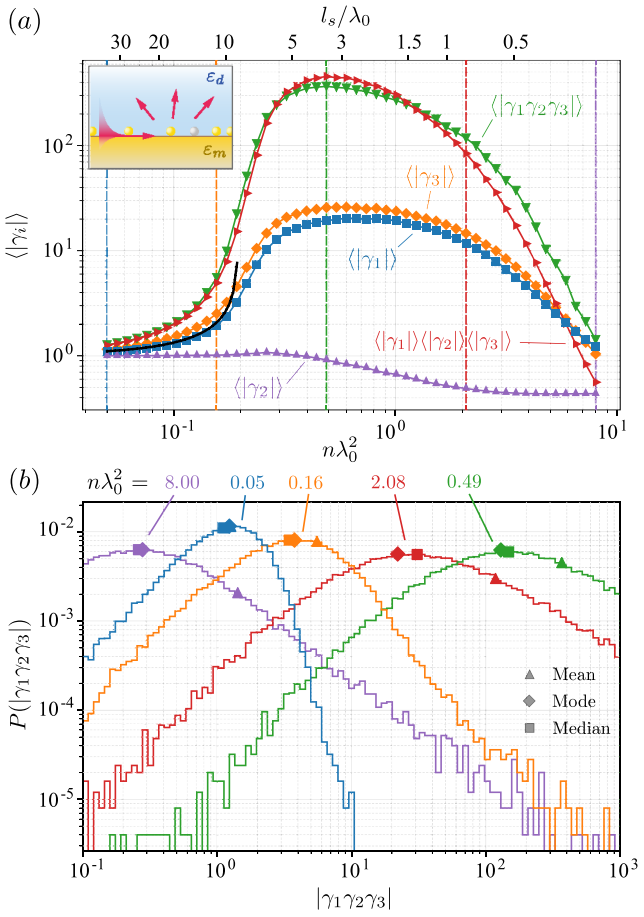

Figure 2. Sensing enhancements. (a) Dependence of $\langle|\gamma_1\gamma_2\gamma_3|\rangle$ (green ▽), $\langle|\gamma_1|\rangle$ (blue □), $\langle|\gamma_2|\rangle$ (purple △), $\langle|\gamma_3|\rangle$ (orange ◇), and $\langle|\gamma_1|\rangle\langle|\gamma_2|\rangle\langle|\gamma_3|\rangle$ (red ▷) on scatterer density n and mean free path l_s for scatterer polarizability $\alpha = \alpha_g$ corresponding to a 40 nm radius gold nanosphere sitting on the surface (z_s = 40 nm). The theoretical result from eq 10 for $\langle|\gamma_1|\rangle$ is also shown (black). Inset shows schematic of SPP scattering from surface bound nanoparticles. (b) Relative frequency/probability distributions for the magnitude of the total enhancement $|\gamma_1\gamma_2\gamma_3|$ for scatterer densities of $n\lambda_0^2 = 0.05$ (blue), 0.16 (orange), 0.49 (green), 2.08 (red), and 8.00 (purple) as also indicated by the corresponding vertical dashed lines in (a). The mean (△), mode (◇), and median (□) for each distribution are also shown.

RESULTS AND DISCUSSION

Our Monte Carlo simulations assumed a free-space wavelength of λ_0 = 650 nm, with ε_d = 1.77 (corresponding to water) and $\varepsilon_m = -13.68 + 1.04i$ (corresponding to gold[51]), such that $k_{SPP} = (1.42 + 0.008i)k_0$ and $|a| = 0.36$. All scatterers were assumed

https://doi.org/10.1021/acsphotonics.1c00725
ACS Photonics 2021, 8, 2227−2233

to be identical ($\alpha_i = \alpha\ \forall\ i$) and located at a height z_s above the metal interface. Their transverse positions were uniformly randomly distributed on the surface over a square area with sides of length L, except for the analyte particle, which was fixed at $\boldsymbol{r}_{N+1} = (0, 0, z_s)$. The number of scatterers remained fixed at $N = 700$, with the scatterer density n adjusted by varying L between $9.4\lambda_0$ and $118\lambda_0$, corresponding to a density ranging from $8\lambda_0^{-2}$ to $0.05\lambda_0^{-2}$. Calculation of the scattered field was performed assuming $\boldsymbol{r}$ was in the far field. Using a stationary phase approximation to evaluate $G(\boldsymbol{r}, \boldsymbol{r}_i)$ in the far-field, reduces these factors, which appear in eq 6, to simple phasors, $G(\boldsymbol{r}, \boldsymbol{r}_{N+1})^{-1}G(\boldsymbol{r}, \boldsymbol{r}_i) = \exp[-i\boldsymbol{k}_{out}\cdot(\boldsymbol{r}_i - \boldsymbol{r}_{N+1})]$, where $\boldsymbol{k}_{out} = \varepsilon_d^{1/2}k_0\hat{\boldsymbol{r}}$ is a wavevector in the direction of $\boldsymbol{r}$. Specifically, the observation position was taken at 70° to the surface normal in the backward x direction ($\boldsymbol{k}_{out} = \varepsilon_d^{1/2}k_0(-\sin 70°, 0, \cos 70°)$). Results showed only a weak dependence on $\boldsymbol{k}_{out}$. The incident field was taken to be a decaying SPP propagating in the x direction of the form $E_{0,z}(x) = \exp(ik_{SPP}x)$. With this form, the ratio of dipole moments in eq 8 reduces to a form $\sim\exp[ik_{SPP}(x_i - x_{N+1})]$, although since k_{SPP} is complex, this factor also describes SPP attenuation. Averages were calculated using 50000 realizations for each density. Convergence plots for the worst case scenario are given in the Supporting Information.

The density dependence of the mean total enhancement $\langle|\gamma_1\gamma_2\gamma_3|\rangle$ and the individual mean enhancement factors $\langle|\gamma_i|\rangle$ are shown in Figure 2a for particle polarizability, $\alpha_g = (3.74 + 0.33i) \times 10^{-32}$ Cm^2 V^{-1}, corresponding to a dressed 40 nm radius gold sphere sat on the gold film ($z_s = 40$ nm). For the given parameters, the density range simulated corresponds to a scattering mean free path varying from $34.3\lambda_0$ down to $0.21\lambda_0$. The mean enhancement factor initially increases with density and rises above 1, indicating that multiple scattering on average enhances the sensitivity at these lower densities. As scatterer density increases further the mean enhancement reaches a maximum of ∼367 at an optimal density of $n = 0.49/\lambda_0^2$ ($l_s = 3.51\lambda_0$), before then decreasing at higher n, eventually dropping below one, indicating that at extremely high densities, multiple scattering acts to decrease the scattered signal perturbation on average. We attribute this decrease to SPP localization[52] effects which restrict the impact of the additional particle to a region of the order of the localization length in size. In particular, we note the localization length of a 2D system can be estimated as $\xi = l_s\exp(\pi\mathrm{Re}[k_{SPP}]l_s/2)$,[53] which becomes comparable to the system size for $l_s \approx 0.73\lambda_0$ in our simulations. Specifically, for $l_s = 0.21\lambda_0$, we have $\xi/L = 0.42$. Note it has been shown that Anderson localization of light cannot be achieved for fully vectorial 3D random ensembles of dipole scatterers such that we would not expect a corresponding decrease in enhancement for such systems.[54] In general, $\langle|\gamma_2|\rangle$ remains close to one, meaning the effect of loop paths is weak compared to $\langle|\gamma_1|\rangle$ and $\langle|\gamma_3|\rangle$, which are of comparable magnitude.

An approximate scaling theory for the behavior of $\langle|\gamma_{1,3}|\rangle$ in the low density regime can be derived by treating the sums in eqs 6 and 8 as random phasor sums. Specifically, when l_s is larger than $\lambda_{SPP} = 2\pi/\mathrm{Re}[k_{SPP}]$, propagation between each scattering event decorrelates the amplitude and phase of each phasor in the sum such that the sums are circular Gaussian random variables with variance $\sigma_{1,3}^2 = N\langle|A_i|^2\rangle/2$, where $|A_i|$ are the amplitudes of the elements of the corresponding sum.[55] The amplitude of $\gamma_{1,3}$ thus follows a Rician distribution with width parameter $\sigma_{1,3}$. For γ_1 we have $A_i = (k_0^2/\varepsilon_0)e^{-i\boldsymbol{k}_{out}\cdot(\boldsymbol{r}_i-\boldsymbol{r}_{N+1})}\sum_j M_{ij}^{-1}\alpha_j G_{j,N+1}$, which represents the sum of all scattering paths from $\boldsymbol{r}_{N+1}$ to $\boldsymbol{r}_i$. In calculating $\langle|A_i|^2\rangle$, the interference of all paths should be considered; however, adopting the ladder approximation (valid when $k_{SPP}l_s \gg 1$), only the interference of identical scattering paths are assumed to contribute to the average owing to the random phase difference between different trajectories.[50] Within this approximation, we find in the limit $N, L \to \infty$ with $n = N/L^2$ fixed (see Supporting Information)

$$\sigma_1^2 = \frac{1}{2}\frac{l_s^{-1}}{l_{abs}^{-1} + 4n\mathrm{Im}(\mu)/(\mathrm{Re}[k_{SPP}]) - l_s^{-1}} \tag{10}$$

In the lossless case ($\mathrm{Im}[k_{SPP}] = 0$) σ_3^2 is identical to σ_1^2. Using the properties of the Rician distribution, the resulting mean magnitude of the enhancement follows as $\langle|\gamma_{1,3}|\rangle = \sigma_{1,3}(\pi/2)^{1/2}L_{1/2}(-1/(2\sigma_{1,3}^2))$, where $L_{1/2}(x)$ is a generalized Laguerre polynomial. Since l_s^{-1} is proportional to n, $\langle|\gamma_1|\rangle$ initially increases from 1 linearly with density, before increasing much more rapidly as l_s approaches l_{abs}. The result diverges when the denominator vanishes, by which point the ladder approximation breaks down and the effects of interference between different paths (such as coherent backscattering) become significant.[50] This behavior is evidenced in Figure 2, with good agreement found between the ladder approximation for $\langle|\gamma_1|\rangle$ and numerical calculations over the range of validity. The density dependence of $\langle|\gamma_3|\rangle$ is analogous; however, the effect of loss (included in the numerical simulations) is to slightly increase $\langle|\gamma_3|\rangle$.

In general, the individual enhancement factors are not statistically independent such that $\langle|\gamma_1\gamma_2\gamma_3|\rangle \neq \langle|\gamma_1|\rangle\langle|\gamma_2|\rangle\langle|\gamma_3|\rangle$, as also shown in Figure 2a. Qualitative agreement between $\langle|\gamma_1\gamma_2\gamma_3|\rangle$ and $\langle|\gamma_1|\rangle\langle|\gamma_2|\rangle\langle|\gamma_3|\rangle$ is clearly apparent, particularly at lower densities; however, correlations cause a noticeable quantitative difference at densities at or beyond the peak. Analysis of the Pearson's correlation coefficients P_{ij} between $|\gamma_i|$ and $|\gamma_j|$ ($i \neq j$), reveals that $|\gamma_2|$ shows little correlation with the other enhancement factors ($P_{12}, P_{23} \in [-0.1, 0.1]$) across the full density range. This is because the loop paths associated with γ_2 are distinct from the scattering paths in $\gamma_{1,3}$. In contrast, scattering trajectories contributing to γ_1 and γ_3 are partially related by reciprocity,[56] such that a multiple scattering path from $\boldsymbol{r}_{N+1}$ to $\boldsymbol{r}_i$ (associated with γ_1) has the same phase and amplitude as the reciprocal path going from $\boldsymbol{r}_i$ to $\boldsymbol{r}_{N+1}$ (associated with γ_3). Correlation of $|\gamma_1|$ and $|\gamma_3|$ is hence dictated by the correlation between the additional propagation phases appearing in each enhancement factor, namely, that of propagation of the scattered (incident) field from (to) the relevant scattering particle. At low densities, these propagation phases remain uncorrelated ($|P_{13}| \lesssim 0.1$ for $n\lambda_0^2 \lesssim 0.1$); however, at higher densities, the typically shorter distances between scattering sites and the analyte particle mean the phase difference of the incident and outgoing fields are smaller, resulting in increased correlation ($P_{13} \in [0.6, 0.8]$ for $n\lambda_0^2 > 0.2$).

Histograms of the relative frequency of $|\gamma_1\gamma_2\gamma_3|$, shown in Figure 2b, demonstrate that at low densities the distribution of total enhancements is tightly centered around ∼1. At densities close to the optimum value, the probability distribution however exhibits a long tail. A given scattering configuration at the optimum density consequently has a high probability of producing a significant sensitivity enhancement; however, it should be noted that the total enhancement for a given

https://doi.org/10.1021/acsphotonics.1c00725
ACS Photonics 2021, 8, 2227−2233

realization will likely be smaller than the mean total enhancement (mode ≈ median ≪ mean), typically ∼100. Importantly, there is a small but non-negligible probability of a very large enhancement even as high as $\sim 10^3$. At the highest densities, the majority of realizations suppress sensitivity, albeit the tail is still longer relative to the lowest densities. Consequently, even though the mean enhancements for the two limiting cases are both of order unity, for high scatterer density there exist a small number of configurations that produce an appreciable sensitivity enhancement. In contrast, at low densities, different configurations do not differ greatly in their effect on sensitivity.

Importantly, eqs 6−8 predict that the statistics of the total enhancement are sensitive to the phase of μ by virtue of the αG_{ij} factors. Physically, this parameter can be tuned in multiple ways. Variation of either the material composition or geometrical properties of the individual scatterers can, for example, modify the particle polarizability α. Moreover, for resonant scatterers, such as plasmonic nanoparticles, tuning the operational wavelength provides an additional degree of freedom. Introduction of an index matched spacer layer between the substrate and background scatterers furthermore allows the height z_s to be adjusted. Shifting the phase of μ while holding its amplitude constant leaves both the elastic SPP scattering cross-section and mean free path unchanged, however, results in a change in the absorption cross-section and scattering out of SPPs. Consequently, a different dependence of the mean enhancement on scatterer density is seen as shown in Figure 3 for a phase shift of $\pi/2$. Notably, in this case the mean enhancements are reduced at low densities compared to Figure 2, which we attribute to a reduction in the field incident on scatterers due to increased absorption and scattering out of SPP modes. At higher n, however, the same decay in enhancement with increasing density is seen. The maximum sensitivity enhancement is of similar magnitude (∼119) and occurs at a higher density ($n = 2.31/\lambda_0^2$, $l_s = 0.74\lambda_0$) compared to the gold nanosphere case. Enhancements are furthermore seen to occur over a narrower density range. Good agreement between the ladder approximation for $\langle|\gamma_1|\rangle$ is once more evident, however, $\langle|\gamma_3|\rangle$ is significantly reduced due to the increased role played by absorption. The probability distributions shown in Figure 3b show the same behavior as the gold sphere case in the low, near-optimal, and high density regimes; however, the transition between each regime occurs at different densities. Similarly, P_{ij} shows similar trends as for the gold, although correlations between $|\gamma_1|$ and $|\gamma_3|$ become noticeable at a higher density.

CONCLUSIONS

Using a coupled dipole formalism, we have derived expressions for the multiple scattering based enhancement of the scattered field perturbation when a scatterer is added to a disordered scattering environment. Equations 6−8 apply quite generally to a range of wave scattering phenomena, both vector and scalar, through the appropriate choice of the Green's tensor. The total enhancement factor derives from three contributions, each arising from different sets of multiple scattering paths, hence allowing insight into the physical mechanisms that affect single particle sensitivity in the multiple scattering regime. Although the local density of states (LDOS)[57] is frequently used to assess the effect of spatial inhomogeneity, such as system disorder, on an oscillating dipole, it is important to note that the enhancement factors introduced here capture important

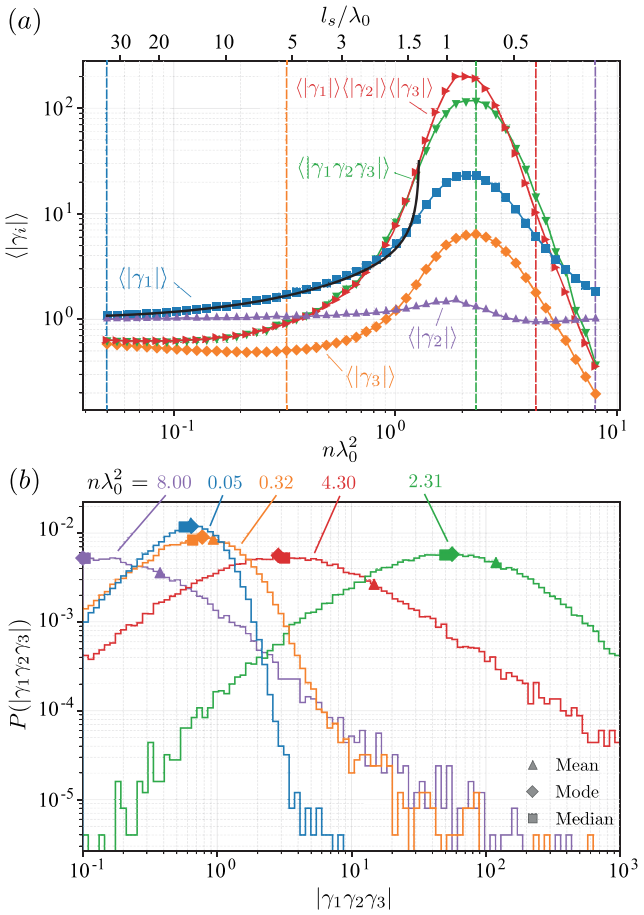

Figure 3. Sensing enhancements for phase-shifted polarizability. As Figure 2 albeit for polarizability $\alpha = \alpha_g e^{i\pi/2}$.

additional features present in the sensing system considered. The LDOS describes the relative power radiated by a dipole in an inhomogeneous environment compared to free space and would hence describe the enhancement for, for example, dark-field scattering based or fluorescence detection;[58] however, in the system considered in this work, particle detection exploits interferometric detection.[4,59] Specifically, the illumination field generates a background field that coherently interferes with the field scattered from an analyte particle. Accordingly, the magnitude of the scattered signal scales as R^3 as opposed to R^6, where R is the analyte particle radius, hence, crucially helping to mitigate noise. Nevertheless, both the LDOS and the enhancement factors of eqs 6−8 derive from the system Green's function and similar features, such as an exponential distance dependence[60] and long-tailed decay,[61,62] are seen.

Based on our model, Monte Carlo simulations of SPP scattering by dipole scatterers randomly distributed on a metal−dielectric interface were performed, which demonstrated that the sensitivity to the addition of a single particle can be enhanced by a factor on the order of 10^2 on average. Moreover, it was shown that there exists an optimum density of scatterers at which the sensitivity gain is maximized. While the optimum density depends on the properties of the individual scatterers, the size of the peak enhancement is relatively insensitive to the individual scatterers. Our results can hence be used to optimize the design of SPP sensors consisting of random nanoscatterers in order to maximize sensitivity. Physically, the optimum scatterer density exists due to the competing effects of dipole

https://doi.org/10.1021/acsphotonics.1c00725
ACS Photonics 2021, 8, 2227−2233

coupling and Anderson localization and would thus be expected in a range of disordered systems beyond the SPP scattering considered in this work. While the former effect typically increases the average scattering perturbation induced by the addition of an analyte particle, the latter confines such perturbations to a smaller spatial region. Optimal configurations would, however, not be expected in scattering systems in which localization is more difficult or cannot be achieved, such as 3D electromagnetic scattering in ensembles of point scatterers.[54]

Finally, we note that the fabrication of nanostructures and deposition of nanoparticles of subwavelength dimensions is becoming more routine, using methods such as electron beam lithography and focused ion beam lithography,[28] such that the dipole approximation made in this work is applicable to realistic experimental systems. Moving beyond dipole scatterers to larger structures does however introduce preferential scattering in the forward direction. Similar anisotropic scattering can also occur for SPP scattering when surface dressing is large.[47] In such scenarios, the transport mean free path $l_{tr} = l_s/(1 + \langle \cos \theta \rangle)$, where $\langle \cos \theta \rangle$ is the average of cosine of the scattering angle,[50] describes the length scale over which the scattering direction is randomized and therefore represents a more suitable parametrization of different scattering regimes. For highly anisotropic scattering, the transport mean free path can however become very long, such that densities required to achieve localization are difficult to reach. Moreover, in systems with loss such as SPP sensors, the absorption length must be longer than the mean free path for multiple scattering effects and localization to play a role. Such factors must therefore also be considered when optimizing the sensitivity of random nanostructured sensors.[42]

■ ASSOCIATED CONTENT

Supporting Information

The Supporting Information is available free of charge at https://pubs.acs.org/doi/10.1021/acsphotonics.1c00725.

Full derivations of eq 10; Simulation convergence plots (PDF)

■ AUTHOR INFORMATION

Corresponding Author

Matthew R. Foreman − *Blackett Laboratory, Imperial College London, London SW7 2BW, United Kingdom;* orcid.org/0000-0001-5864-9636; Email: matthew.foreman@imperial.ac.uk

Author

Joel Berk − *Blackett Laboratory, Imperial College London, London SW7 2BW, United Kingdom*

Complete contact information is available at: https://pubs.acs.org/10.1021/acsphotonics.1c00725

Notes

The authors declare no competing financial interest.

■ ACKNOWLEDGMENTS

This work was funded by the Engineering and Physical Sciences Research Council (EPSRC; 1992728) and the Royal Society (UF150335).

■ REFERENCES

(1) Fan, X.; White, I. M.; Shopova, S. I.; Zhu, H.; Suter, J. D.; Sun, Y. Sensitive optical biosensors for unlabeled targets: A review. *Anal. Chim. Acta* **2008**, *620*, 8.

(2) Zhu, S.; Ma, L.; Wang, S.; Chen, C.; Zhang, W.; Yang, L.; Hang, W.; Nolan, J. P.; Wu, L.; Yan, X. Light-Scattering Detection below the Level of Single Fluorescent Molecules for High-Resolution Characterization of Functional Nanoparticles. *ACS Nano* **2014**, *8*, 10998.

(3) Stetefeld, J.; Mckenna, S. A.; Patel, T. R. Dynamic light scattering: a practical guide and applications in biomedical sciences. *Biophys. Rev.* **2016**, *8*, 409.

(4) Taylor, R. W.; Sandoghdar, V. Interferometric Scattering Microscopy: Seeing Single Nanoparticles and Molecules via Rayleigh Scattering. *Nano Lett.* **2019**, *19*, 4827.

(5) Yang, Y.; Shen, G.; Wang, H.; Li, H.; Zhang, T.; Tao, N.; Ding, X.; Yu, H. Interferometric plasmonic imaging and detection of single exosomes. *Proc. Natl. Acad. Sci. U. S. A.* **2018**, *115*, 10275.

(6) Zhang, P.; Ma, G.; Dong, W.; Wan, Z.; Wang, S.; Tao, N. Plasmonic scattering imaging of single proteins and binding kinetics. *Nat. Methods* **2020**, *17*, 1010.

(7) Ferreira, J.; Santos, M. J. L.; Rahman, M. M.; Brolo, A. G.; Gordon, R.; Sinton, D.; Girotto, E. M. Attomolar protein detection using in-hole surface plasmon resonance. *J. Am. Chem. Soc.* **2009**, *131*, 436−437.

(8) Liu, X.; Huo, Q. A washing-free and amplification-free one-step homogeneous assay for protein detection using gold nanoparticle probes and dynamic light scattering. *J. Immunol. Methods* **2009**, *349*, 38−44.

(9) Lee, S.; Ahn, S.; Chakkarapani, S. K.; Kang, S. H. Supersensitive Detection of the Norovirus Immunoplasmon by 3D Total Internal Reflection Scattering Defocus Microscopy with Wavelength-Dependent Transmission Grating. *ACS Sensors* **2019**, *4*, 2515−2523.

(10) Zhao, X.; Tapec-Dytioco, R.; Tan, W. Ultrasensitive DNA detection using highly fluorescent bioconjugated nanoparticles. *J. Am. Chem. Soc.* **2003**, *125*, 11474−11475.

(11) Li, N.; Chen, H.; Zhang, M.; Zha, Y.; Mu, Z.; Ma, Y.; Chen, P. A universal ultrasensitive platform for enzyme-linked immunoassay based on responsive surface-enhanced Raman scattering. *Sens. Actuators, B* **2020**, *315*, 128135.

(12) Badon, A.; Boccara, A. C.; Lerosey, G.; Fink, M.; Aubry, A. Multiple scattering limit in optical microscopy. *Opt. Express* **2017**, *25*, 28914.

(13) Yoon, S.; Kim, M.; Jang, M.; Choi, Y.; Choi, W.; Kang, S.; Choi, W. Deep optical imaging within complex scattering media. *Nat. Rev. Phys.* **2020**, *2*, 141.

(14) Bar-Ziv, R.; Meller, A.; Tlusty, T.; Moses, E.; Stavans, J.; Safran, S. A. Localized Dynamic Light Scattering: Probing Single Particle Dynamics at the Nanoscale. *Phys. Rev. Lett.* **1997**, *78*, 154.

(15) Pine, D. J.; Weitz, D. A.; Chaikin, P. M.; Herbolzheimer, E. Diffusing wave spectroscopy. *Phys. Rev. Lett.* **1988**, *60*, 1134.

(16) Mosk, A. P.; Lagendijk, A.; Lerosey, G.; Fink, M. Controlling waves in space and time for imaging and focusing in complex media. *Nat. Photonics* **2012**, *6*, 283.

(17) Choi, Y.; Yang, T. D.; Fang-Yen, C.; Kang, P.; Lee, K. J.; Dasari, R. R.; Feld, M. S.; Choi, W. Overcoming the diffraction limit using multiple light scattering in a highly disordered medium. *Phys. Rev. Lett.* **2011**, *107*, 023902.

(18) Berkovits, R. Sensitivity of the multiple scattering speckle pattern to the motion of a single scatterer. *Phys. Rev. B: Condens. Matter Mater. Phys.* **1991**, *43*, 8638.

(19) Nieuwenhuizen, T. M.; van Rossum, M. C. W. Role of a single scatterer in a multiple scattering medium. *Phys. Lett. A* **1993**, *177*, 102.

(20) Berkovits, R.; Feng, S. Theory of speckle pattern tomography in multiple scattering media. *Phys. Rev. Lett.* **1990**, *65*, 3120.

(21) den Outer, P. N.; Nieuwenhuizen, T. M.; Lagendijk, A. Location of objects in multiple-scattering media. *J. Opt. Soc. Am. A* **1993**, *10*, 1209.

(22) Huang, Y.; Ma, L.; Li, J.; Zhang, Z. Nanoparticle-on-mirror cavity modes for huge and/or tunable plasmonic field enhancement. *Nanotechnology* **2017**, *28*, 105203.
(23) Baumberg, J. J.; Aizpurua, J.; Mikkelsen, M. H.; Smith, D. R. Extreme nanophotonics from ultrathin metallic gaps. *Nat. Mater.* **2019**, *18*, 668.
(24) Cang, H.; Labno, A.; Lu, C.; Yin, X.; Liu, M.; Gladden, C.; Liu, Y.; Zhang, X. Probing the electromagnetic field of a 15-nanometre hotspot by single molecule imaging. *Nature* **2011**, *469*, 385.
(25) Alonso-González, P.; Albella, P.; Schnell, M.; Chen, J.; Huth, F.; García-Etxarri, A.; Casanova, F.; Golmar, F.; Arzubiaga, L.; Hueso, L. E.; Aizpurua, J.; Hillenbrand, R. Resolving the electromagnetic mechanism of surface-enhanced light scattering at single hot spots. *Nat. Commun.* **2012**, *3*, 684.
(26) Liu, H.; Yang, Z.; Meng, L.; Sun, Y.; Wang, J.; Yang, L.; Liu, J.; Tian, Z. Three-Dimensional and Time-Ordered Surface-Enhanced Raman Scattering Hotspot Matrix. *J. Am. Chem. Soc.* **2014**, *136*, 5332.
(27) Itoh, T.; Yamamoto, Y. S.; Kitahama, Y.; Balachandran, J. One-dimensional plasmonic hotspots located between silver nanowire dimers evaluated by surface-enhanced resonance Raman scattering. *Phys. Rev. B: Condens. Matter Mater. Phys.* **2017**, *95*, 115441.
(28) Stewart, M. E.; Anderton, C. R.; Thompson, L. B.; Maria, J.; Gray, S. K.; Rogers, J. A.; Nuzzo, R. G. Nanostructured plasmonic sensors. *Chem. Rev.* **2008**, *108*, 494.
(29) Konopsky, V. N.; Alieva, E. V. Photonic crystal surface mode imaging biosensor based on wavelength interrogation of resonance peak. *Sens. Actuators, B* **2018**, *276*, 271.
(30) Segev, M.; Silberberg, Y.; Christodoulides, D. N. Anderson localization of light. *Nat. Photonics* **2013**, *7*, 197.
(31) Maystre, D.; Saillard, M. Localization of light by randomly rough surfaces: concept of localization. *J. Opt. Soc. Am. A* **1994**, *11*, 680.
(32) Boguslawski, M.; Brake, S.; Leykam, D.; Desyatnikov, A. S.; Denz, C. Observation of transverse coherent backscattering in disordered photonic structures. *Sci. Rep.* **2017**, *7*, 10439.
(33) Berkovits, R.; Feng, S. Correlations in coherent multiple scattering. *Phys. Rep.* **1994**, *238*, 135.
(34) Juette, M. F.; Terry, D. S.; Wasserman, M. R.; Altman, R. B.; Zhou, Z.; Zhao, H.; Blanchard, S. C. Single-molecule imaging of non-equilibrium molecular ensembles on the millisecond timescale. *Nat. Methods* **2016**, *13*, 341−344.
(35) Jahn, M.; Buchner, J.; Hugel, T.; Rief, M. Folding and assembly of the large molecular machine Hsp90 studied in single-molecule experiments. *Proc. Natl. Acad. Sci. U. S. A.* **2016**, *113*, 1232−1237.
(36) Novotny, L.; Hecht, B.; Pohl, D. W. Interference of locally excited surface plasmons. *J. Appl. Phys.* **1997**, *81*, 1798.
(37) Chaumet, P. C.; Rahmani, A.; Sentenac, A.; Bryant, G. W. Efficient computation of optical forces with the coupled dipole method. *Phys. Rev. E* **2005**, *72*, 046708.
(38) Søndergaard, T.; Bozhevolnyi, S. I. Vectorial model for multiple scattering by surface nanoparticles via surface polariton-to-polariton interactions. *Phys. Rev. B: Condens. Matter Mater. Phys.* **2003**, *67*, 165405.
(39) Novotny, L.; Hecht, B. *Principles of Nano-Optics*; Cambridge University Press, 2006.
(40) Lakhtakia, A. Macroscopic theory of the coupled dipole approximation method. *Opt. Commun.* **1990**, *79*, 1.
(41) Huang, J. A perturbative multiple scattering theory. *Phys. Lett. A* **2004**, *322*, 10.
(42) Berk, J.; Foreman, M. R. Role of Multiple Scattering in Single Particle Perturbations in Absorbing Random Media. *Phys. Rev. Research*, **2021**, in press, accepted manuscript.
(43) Golub, G. H.; Van Loan, C. F. *Matrix Computations*; Johns Hopkins University Press, 1996.
(44) Homola, J. Present and future of surface plasmon resonance biosensors. *Anal. Bioanal. Chem.* **2003**, *377*, 528.
(45) van Beijnum, F.; Sirre, J.; Rétif, C.; van Exter, M. P. Speckle correlation functions applied to surface plasmons. *Phys. Rev. B: Condens. Matter Mater. Phys.* **2012**, *85*, 035437.
(46) Berk, J.; Paterson, C.; Foreman, M. R. Tracking Single Particles using Surface Plasmon Leakage Radiation Speckle. *J. Lightwave Technol.* **2021**, *39*, 3950.
(47) Evlyukhin, A. B.; Bozhevolnyi, S. I. Point-dipole approximation for surface plasmon polariton scattering: Implications and limitations. *Phys. Rev. B: Condens. Matter Mater. Phys.* **2005**, *71*, 134304.
(48) Bozhevolnyi, S. I.; Coello, V. Elastic scattering of surface plasmon polaritons: Modeling and experiment. *Phys. Rev. B: Condens. Matter Mater. Phys.* **1998**, *58*, 10899.
(49) Søndergaard, T.; Bozhevolnyi, S. I. Surface plasmon polariton scattering by a small particle placed near a metal surface: An analytical study. *Phys. Rev. B: Condens. Matter Mater. Phys.* **2004**, *69*, 045422.
(50) Akkermans, E.; Montambaux, G. *Mesoscopic Physics of Electrons and Photons*, 1st ed; Cambridge University Press, 2007.
(51) Johnson, P. B.; Christy, R. W. Optical constants of the noble metals. *Phys. Rev. B* **1972**, *6*, 4370.
(52) Zhu, Y.; Jing, H.; Peng, R. W.; Li, C. Y.; He, J.; Xiong, B.; Wang, M. Realizing Anderson localization of surface plasmon polaritons and enhancing their interactions with excitons in 2D disordered nanostructures. *Appl. Phys. Lett.* **2020**, *116*, 201106.
(53) Sheng, P. *Introduction to Wave Scattering, Localization and Mesoscopic Phenomena*; Academic Press Inc.: New York, 1995.
(54) Skipetrov, S. E.; Sokolov, I. M. Absence of Anderson localization of light in a random ensemble of point scatterers. *Phys. Rev. Lett.* **2014**, *112*, 023905.
(55) Goodman, J. *Speckle Phenomena in Optics: Theory and Applications*; Roberts & Company, 2007.
(56) Byrnes, N.; Foreman, M. R. Symmetry constraints for vector scattering and transfer matrices containing evanescent components: energy conservation, reciprocity and time reversal. *Phys. Rev. Res.* **2021**, *3*, 013129.
(57) Carminati, R.; Cazé, A.; Cao, D.; Peragut, F.; Krachmalnicoff, V.; Pierrat, R.; De Wilde, Y. Electromagnetic density of states in complex plasmonic systems. *Surf. Sci. Rep.* **2015**, *70*, 1.
(58) Weigel, A.; Sebesta, A.; Kukura, P. Dark Field Micro-spectroscopy with Single Molecule Fluorescence Sensitivity. *ACS Photonics* **2014**, *1*, 848.
(59) Ignatovich, F. V.; Novotny, L. Real-time and background-free detection of nanoscale particles. *Phys. Rev. Lett.* **2006**, *96*, 013901.
(60) Castanié, E.; Krachmalnicoff, V.; Cazé, A.; Pierrat, R.; De Wilde, Y.; Carminati, R. Distance dependence of the local density of states in the near field of a disordered plasmonic film. *Opt. Lett.* **2012**, *37*, 3006.
(61) Riboli, F.; Uccheddu, F.; Monaco, G.; Caselli, N.; Intonti, F.; Gurioli, M.; Skipetrov, S. E. Tailoring Correlations of the Local Density of States in Disordered Photonic Materials. *Phys. Rev. Lett.* **2017**, *119*, 043902.
(62) Krachmalnicoff, V.; Castanié, E.; De Wilde, Y.; Carminati, R. Fluctuations of the local density of states probe localized surface plasmons on disordered metal films. *Phys. Rev. Lett.* **2010**, *105*, 183901.

https://doi.org/10.1021/acsphotonics.1c00725
ACS Photonics 2021, 8, 2227−2233